Available online at www.sciencedirect.com

ScienceDirect

IFAC Papers Online CONFERENCE PAPER ARCHIVE

IFAC PapersOnLine 51-2 (2018) 403–408

Reduced Models for the Static Simulation of an Elastic Continuum Mechanism

Bastian Deutschmann * **Simon R. Eugster** ** **Christian Ott** *

* *Institute of Robotics and Mechatronics, DLR (e-mail: {bastian.deutschmann, christian.ott}@dlr.de)*
** *Institute for Nonlinear Mechanics (e-mail: simon.eugster@inm.uni-stuttgart.de)*

Abstract: In this paper, two approaches are established and compared that simulate the static deformation of a tendon-driven, elastic continuum mechanism (ECM). The mechanism at hand is made out of silicon and deforms in a large workspace as a results of any externally applied wrench. This yields high dexterity and high mechanical robustness for the system, but also the commonly used kinematic model is not suitable any more. The discussed models in this paper are essentially different. At first, the finite element method (FEM) is used to discretize the mechanism along its centerline. A nonlinear material law is setup and identified for the axial direction and it could be shown that the established model matches the real system very closely. The second model is more abstract. Here, a polynomial relationship is setup between the Cartesian pose of the mechanism and the associated wrench necessary to achieve this deflection. A comparison between the two models show, that the FEM model is slower but more accurate and therefore useful for offline computations whereas the polynomial model seems more suitable for real-time control approaches, with an acceptable accuracy and an efficient computation.

Keywords: Robotics, Model-Reduction

1. INTRODUCTION

The system at hand consists of an elastic continuum mechanism (ECM) made out of silicon and is a planar version of the mechanism described in [8]. While one side of the mechanism is fixed to the ground, on top of the other side a robot head is mounted. The planar mechanism is actuated by two tendons in an antagonistic fashion. The tendons are connected to the head-plate at each side. By pulling at both tendons, a combined loading is exerted onto the ECM to move the head into the desired direction. The required kinematical and statical quantities of the system model are depicted in Fig. 1.
The common approach to reduce the model complexity is to assume that the center line of the mechanism deforms like a circular arc, see e.g. [1]. With that, the geometry of the deformation is heavily simplified and the static equations can be solved analytically. Based on that assumption, [5] establish experimentally a bending stiffness, whereas [7] utilizes the manufacturing data for their steel continuum. If such a kinematic mapping cannot be used due to changing loading conditions onto the system, so called geometrically exact models, e.g. [9], which are usually computationally expensive are applied. Another approach is to hide the geometry of the deformation and the material properties within a mapping that needs to be identified. [6] teaches a neural network to relate actuation forces to static Cartesian positions in the reachable workspace of the manipulator. The model proved to be computationally efficient and it was able to accurately predict the position of the manipulator.

In this paper, we introduce a model-based on a nonlinear beam formulation which can be solved using the Finite Element Method (FEM). An alternative approach is proposed in [2] which aims at a computational efficient model. The assumption is that the Cartesian pose at the end of the ECM is enough to describe the deformation behavior which reduces the model of the ECM to a nonlinear Cartesian spring. In [3], an experimental procedure is explained with which such a nonlinear spring can be identified experimentally as a mapping from the Cartesian pose to the Cartesian wrench using multivariate polynomials.
The present work aims to compare the two aforementioned models for a tendon-driven ECM. In the first part, the FEM model together with the experimental identification of the stiffness parameters, as e.g. the bending stiffness, are discussed. In the second part, the identification procedure for the polynomials is summarized. For brevity, we will focus here only on the planar case, see Fig. 1, although, the polynomial mapping is easily extendable to the spatial case [3]. In contrast, a spatial FEM model can be derived by the discussed formalism of this work. However, the discretization and interpolation of the rotation parametrization for the spatial model is not trivial and needs special treatment.

The main contribution of this work is twofold: To the best of the authors knowledge, this is the first work that establishes a nonlinear FEM model of a tendon-driven ECM with nonlinear input coupling and nonlinear material law in the compression direction. Second, the polynomial model is compared with the FEM model using experimental data regarding accuracy and computation time.

2. FINITE ELEMENT MODEL

The deformation of the system is embedded in the Euclidean three-space $\mathbb{E}^3$ with origin O and coordinate frame $\boldsymbol{e}_i^I \in \mathbb{E}^3, i = \{x, y, z\}$ and takes place exclusively in the $\boldsymbol{e}_x^I$-$\boldsymbol{e}_z^I$-plane. The ECM is modeled as a planar nonlinear Timoshenko beam. According to the Timoshenko beam assumptions, the deformation of the three-dimensional continuum can be described only by the deformation of a centerline and the rotations of plane rigid cross-sections attached to every point of the centerline. The centerline $\boldsymbol{r} = \boldsymbol{r}(\nu) \in \mathbb{E}^3$ is a curve parameterized by $\nu = [0, L] \subset \mathbb{R}$,

2405-8963
Peer review under responsibility of International Federation of Automatic Control.
10.1016/j.ifacol.2018.03.069

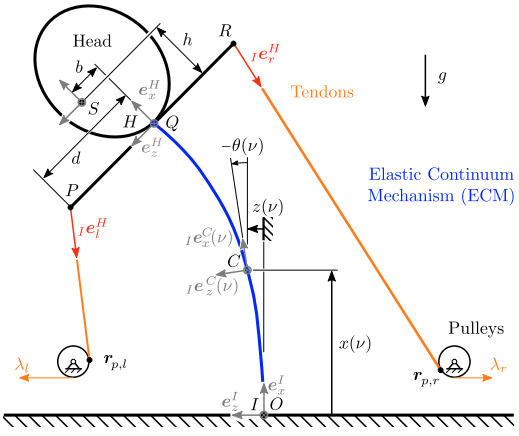

Fig. 1. Schematic drawing of the system.

where ν is the arclength of the undeformed beam with length L. The cross-sections of the beam are represented by the cross-section-fixed frames $\boldsymbol{e}_i^C = \boldsymbol{e}_i^C(\nu) \in \mathbb{E}^3, i = \{x, y, z\}$ continuously varying along the centerline. The beam is fixed to the ground such that $\boldsymbol{r}(0) = 0$ and $\boldsymbol{e}_i^C(0) = \boldsymbol{e}_i^I, i = \{x, y, z\}$. On top of the beam at $\nu = L$ a rigid and massless plate with a width of $2d$ is attached. In P and R two massless tendons are connected to the plate. Both tendons are redirected by a pulley and subjected at their ends to the tensile forces $\lambda_l \geq 0$ and $\lambda_r \geq 0$, respectively. The head is modeled as a rigid body with center of mass (CoM) S, mass m_H and is rigidly connected to the beam in Q such that head-fixed frame $\boldsymbol{e}_i^H := \boldsymbol{e}_i^C(L), i = \{x, y, z\}$.

The Cartesian coordinate representation of a vector $\boldsymbol{a} \in \mathbb{E}^3$ in an arbitrary orthonormal B-system rotated against the I-system is denoted as ${}_B\boldsymbol{a} = (a_x^B\, a_y^B\, a_z^B)^T \in \mathbb{R}^3$ with $\boldsymbol{a} = a_x^B \boldsymbol{e}_x^B + a_y^B \boldsymbol{e}_y^B + a_z^B \boldsymbol{e}_z^B \in \mathbb{E}^3$. The orthogonal transformation matrix $\boldsymbol{A}_{IB} \in \mathbb{R}^{3\times3}$ relates the respective coordinates in accordance with ${}_I\boldsymbol{a} = \boldsymbol{A}_{IB}\,{}_B\boldsymbol{a}$ and corresponds with the coordinates of the B-frame basis vectors in the I-system, i.e. $\boldsymbol{A}_{IB} = ({}_I\boldsymbol{e}_x^B\ {}_I\boldsymbol{e}_y^B\ {}_I\boldsymbol{e}_z^B) \in \mathbb{R}^{3\times3}$. The inverse of the transformation matrix $\boldsymbol{A}_{IB}$ is denoted as $\boldsymbol{A}_{BI} = \boldsymbol{A}_{IB}^{-1} = \boldsymbol{A}_{IB}^T$.

2.1 Kinematics

The centerline $\boldsymbol{r}(\nu)$ and the basis vectors of the cross-section-fixed frames $\boldsymbol{e}_i^C(\nu)$ are represented in the I-system as

$$ {}_I\boldsymbol{r}(\nu) = \begin{pmatrix} x(\nu) \\ 0 \\ z(\nu) \end{pmatrix}, \quad \boldsymbol{A}_{IC}(\nu) = \begin{pmatrix} \cos\theta(\nu) & 0 & \sin\theta(\nu) \\ 0 & 1 & 0 \\ -\sin\theta(\nu) & 0 & \cos\theta(\nu) \end{pmatrix}, \tag{1} $$

and determined by the real-valued generalized position functions $x = x(\nu)$, $z = z(\nu)$ and $\theta = \theta(\nu)$. Hence, the position vector $\boldsymbol{r}_{OQ}$ and the basis vectors of the H-system are given in the I-system by

$$ {}_I\boldsymbol{r}_{OQ} = {}_I\boldsymbol{r}(L), \quad \boldsymbol{A}_{IH} = \boldsymbol{A}_{IC}(L). \tag{2} $$

With (2) and the dimensions from Fig. 1, the position of the CoM of the head is

$$ {}_I\boldsymbol{r}_{OS} = {}_I\boldsymbol{r}_{OQ} + h\,{}_I\boldsymbol{e}_x^H + b\,{}_I\boldsymbol{e}_z^H. \tag{3} $$

The change of the cross-section orientation along ν is described by the material curvature, the skew-symmetric matrix

$$ {}_I\hat{\boldsymbol{k}}_{IC}(\nu) = \boldsymbol{A}_{IC}'(\nu)\boldsymbol{A}_{IC}^T(\nu) \in \mathbb{R}^{3\times3} \tag{4} $$

which appears in the expression

$$ ({}_I\boldsymbol{e}_x^C)' = (\boldsymbol{A}_{IC}\boldsymbol{e}_x^C)' = \boldsymbol{A}_{IC}'\boldsymbol{A}_{IC}^T\,{}_I\boldsymbol{e}_x^C = {}_I\hat{\boldsymbol{k}}_{IC}\,{}_I\boldsymbol{e}_x^C \tag{5} $$

and holds analogously for the ${}_I\boldsymbol{e}_y^C$- and ${}_I\boldsymbol{e}_z^C$-direction. Note that $(\bullet)'$ denotes the derivative with respect to the argument. Inserting (1) into (4), straightforward computation leads to the material curvature vector

$$ {}_I\boldsymbol{k}_{IC}(\nu) = ({}_I\hat{\boldsymbol{k}}_{IC}(\nu))^{\check{}} = (\,0\ \theta'(\nu)\ 0\,)^T. \tag{6} $$

Virtual Displacements and Rotations Let $\bar{x} = \bar{x}(\nu, \varepsilon)$, $\bar{z} = \bar{z}(\nu, \varepsilon)$ and $\bar{\theta} = \bar{\theta}(\nu, \varepsilon)$ be variational families of the generalized position functions, i.e. differentiable parameterizations with respect to a parameter $\varepsilon \in \mathbb{R}$ such that the actual positions (we are looking for) are embedded in the family and are obtained for $\varepsilon = \varepsilon_0$. Inserting these functions in (1), the variational families $\bar{\boldsymbol{r}} = \bar{\boldsymbol{r}}(\nu, \varepsilon)$ and $\bar{\boldsymbol{A}}_{IC} = \bar{\boldsymbol{A}}_{IC}(\nu, \varepsilon)$ are induced. The virtual displacement of the centerline $\delta\boldsymbol{r}$ and the virtual rotations of the cross-sections $\delta\boldsymbol{\phi}_{IC}$ are then defined by

$$ {}_I\delta\boldsymbol{r} = \left.\frac{\partial\,{}_I\bar{\boldsymbol{r}}}{\partial\varepsilon}\right|_{\varepsilon=\varepsilon_0}, \quad {}_I\delta\hat{\boldsymbol{\phi}}_{IC} = \left.\frac{\partial\bar{\boldsymbol{A}}_{IC}}{\partial\varepsilon}\right|_{\varepsilon=\varepsilon_0} \boldsymbol{A}_{IC}^T. \tag{7} $$

Explicit computation using (1) and (2) gives

$$ {}_I\delta\boldsymbol{r}(\nu) = (\,\delta x(\nu)\ 0\ \delta z(\nu)\,)^T, \ {}_I\delta\boldsymbol{r}_Q = (\,\delta x_L\ 0\ \delta z_L\,)^T, \tag{8} $$

where $\delta x_L = \delta x(L)$, $\delta z_L = \delta z(L)$. Analogously to the material curvature vector (6), computation of the second equality in (7) leads to the virtual rotation vector

$$ {}_I\delta\boldsymbol{\phi}_{IC}(\nu) = ({}_I\delta\hat{\boldsymbol{\phi}}_{IC}(\nu))^{\check{}} = (\,0\ \delta\theta(\nu)\ 0\,)^T. \tag{9} $$

To establish the virtual work of the external forces acting onto the system, we will need the virtual displacement of the CoM and the virtual displacements of the tendon connection points which are for $\delta\theta_L = \delta\theta(L)$

$$ {}_I\delta\boldsymbol{r}_S = {}_I\delta\boldsymbol{r}_Q + \delta\theta_L\,{}_I\boldsymbol{e}_y^H \times (h\,{}_I\boldsymbol{e}_x^H + b\,{}_I\boldsymbol{e}_z^H), \tag{10} $$

$$ {}_I\delta\boldsymbol{r}_P = {}_I\delta\boldsymbol{r}_Q + \delta\theta_L\,{}_I\boldsymbol{e}_y^H \times d\,{}_I\boldsymbol{e}_z^H, \tag{11} $$

$$ {}_I\delta\boldsymbol{r}_R = {}_I\delta\boldsymbol{r}_Q - \delta\theta_L\,{}_I\boldsymbol{e}_y^H \times d\,{}_I\boldsymbol{e}_z^H. \tag{12} $$

Strain Measures The strain measures are defined as the centerline's tangent in the cross-section-fixed C-system

$$ {}_C\boldsymbol{\gamma}(\nu) = \left(\,\gamma_x^C(\nu)\ 0\ \gamma_z^C(\nu)\,\right)^T = \boldsymbol{A}_{IC}^T(\nu)\,{}_I\boldsymbol{r}'(\nu) \tag{13} $$

together with the material curvature vector in the C-system

$$ {}_C\boldsymbol{k}_{IC}(\nu) = \boldsymbol{A}_{IC}^T(\nu)\,{}_I\boldsymbol{k}_{IC}(\nu) = (\,0\ \theta'(\nu)\ 0\,)^T. \tag{14} $$

2.2 Static Equilibrium Equations of the System

To determine the equilibrium equations of the system, we use the principle of virtual work which postulates that the total virtual work δW^{tot} of the system is zero for all admissible virtual displacements. For static equilibrium, the total virtual work is composed of internal and external virtual work contributions δW^{int} and δW^{ext}, respectively. For the system at hand this results in the requirement

$$ \delta W^{\text{tot}} = \delta W^{\text{int}} + \delta W^{\text{ext}} = 0 \quad \forall \delta\boldsymbol{r}_{\text{adm}}, \delta\boldsymbol{\phi}_{IC,\text{adm}} \tag{15} $$

whereas the admissible virtual displacements and rotations are given by the ones of (7), (8) and (9) which additionally respect the clamping condition at $\nu = 0$, i.e. ${}_I\delta\boldsymbol{r}_{\text{adm}}(0) = 0$ and ${}_I\delta\boldsymbol{\phi}_{IC,\text{adm}}(0) = 0$. In the following, we introduce all virtual work contributions of the system.

Virtual work of internal forces The only internal forces of the system come from the nonlinear Timoshenko beam whose internal virtual work contribution is according to [4] given by

$$\delta W^{\text{int}} = -\int_0^L \big\{ {}_I\boldsymbol{n}^T \left({}_I\delta\boldsymbol{r}' - {}_I\delta\boldsymbol{\phi}_{IC} \times {}_I\boldsymbol{r}' \right) + {}_I\boldsymbol{m}^T {}_I\delta\boldsymbol{\phi}'_{IC} \big\} \mathrm{d}\nu. \tag{16}$$

Therein the resultant contact forces $\boldsymbol{n} = \boldsymbol{n}(\nu) \in \mathbb{E}^3$ and resultant contact couples $\boldsymbol{m} = \boldsymbol{m}(\nu) \in \mathbb{E}^3$ can be identified. Since for the planar system the contact force in $\boldsymbol{e}_y^I$-direction does not contribute to the virtual work, only the contact forces in $\boldsymbol{e}_x^I$- and $\boldsymbol{e}_z^I$-direction are of interest. These can be expressed as

$${}_I\boldsymbol{n}(\nu) = \begin{pmatrix} n_x^I(\nu) \\ * \\ n_z^I(\nu) \end{pmatrix} = \boldsymbol{A}_{ICC}\boldsymbol{n}(\nu) = \boldsymbol{A}_{IC} \begin{pmatrix} N(\nu) \\ 0 \\ Q(\nu) \end{pmatrix}, \tag{17}$$

where $N = N(\nu) \in \mathbb{R}$ and $Q = Q(\nu) \in \mathbb{R}$ are the normal and shear forces acting at each cross-section. In the contact couple ${}_I\boldsymbol{m}(\nu) = (* \; M(\nu) \; *)^T$ only the $\boldsymbol{e}_y^I$-direction with the bending moment $M = M(\nu) \in \mathbb{R}$ is relevant. Using the planar kinematics (8) and (9) together with the just introduced contact forces and couples, the internal virtual work expression (16) takes the form

$$\delta W^{\text{int}} = -\int_0^L \big\{ \delta x' n_x^I + \delta z' n_z^I - \delta\theta(z' n_x^I - x' n_z^I) + \delta\theta' M \big\} \mathrm{d}\nu. \tag{18}$$

The constitutive laws describing the material behavior of the beam are formulated between force and strain components of the cross-section-fixed C-system, i.e.

$$N = \frac{EA}{3}\left(\gamma_x^C - \frac{1}{(\gamma_x^C)^2}\right), \; Q = GA\gamma_z^C, \; M = EI\theta', \tag{19}$$

with the axial stiffness $EA \in \mathbb{R}$, the shear stiffness $GA \in \mathbb{R}$ and the bending stiffness $EI \in \mathbb{R}$. Note the nonlinear Neo-Hookean material law for the normal force which takes into account the experimentally observed stiffening behavior of the material in compression. Linearization around the undeformed configuration, i.e. $\gamma_x^C = 1$, leads directly to Hooke's law $N = EA(\gamma_x^C - 1)$.

Virtual work of external forces The virtual work contributions of the external forces of the system is additively composed of the virtual work due to gravity and the virtual work of the tendon actuation,

$$\delta W^{\text{ext}} = \delta W^{\text{ext,g}} + \delta W^{\text{ext,t}}. \tag{20}$$

For a cross-section density ρA, the virtual work due to gravity with gravity constant g

$$\delta W^{\text{ext,g}} = \int_0^L -(\rho A g \; 0 \; 0)_I \delta\boldsymbol{r} \mathrm{d}\nu - (m_H g \; 0 \; 0)_I \delta\boldsymbol{r}_S, \tag{21}$$

can be further simplified using (10) to

$$\delta W^{\text{ext,g}} = \int_0^L -(\rho A g \; 0 \; 0)_I \delta\boldsymbol{r} \mathrm{d}\nu - m_H g \delta x_L - m_H g \delta\theta_L ({}_I\boldsymbol{e}_x^I)^T ({}_I\boldsymbol{e}_y^H \times (h_I {}_I\boldsymbol{e}_x^H + b_I {}_I\boldsymbol{e}_z^H)). \tag{22}$$

The virtual work of the tendon actuation

$$\delta W^{\text{ext,t}} = \lambda_l {}_I\boldsymbol{e}_l^T {}_I\delta\boldsymbol{r}_P + \lambda_R {}_I\boldsymbol{e}_r^T {}_I\delta\boldsymbol{r}_R \tag{23}$$

is rewritten using (11) and (12) to

$$\delta W^{\text{ext,t}} = (\delta x \; 0 \; \delta z)\Big({}_I\boldsymbol{e}_l \;\; {}_I\boldsymbol{e}_r\Big)\boldsymbol{\lambda} + \delta\theta ({}_I\boldsymbol{e}_y^H)^T \Big(d_I {}_I\boldsymbol{e}_z^H \times {}_I\boldsymbol{e}_l \;\; -d_I {}_I\boldsymbol{e}_z^H \times {}_I\boldsymbol{e}_r\Big)\boldsymbol{\lambda} \tag{24}$$

with the tendon force vector $\boldsymbol{\lambda} = (\lambda_l \;\; \lambda_r)^T$ and the unit tendon direction vectors for left ${}_I\boldsymbol{e}_l^H \in \mathbb{R}^3$ and right ${}_I\boldsymbol{e}_r^H \in \mathbb{R}^3$ tendon as depicted in Fig. 1, i.e.

$$\begin{aligned} {}_I\boldsymbol{e}_l^H &= \left(e_{l,x}^I \; 0 \; e_{l,z}^I \right)^T = {}_I\boldsymbol{r}_{p,l} - {}_I\boldsymbol{r}_P / \| {}_I\boldsymbol{r}_{p,l} - {}_I\boldsymbol{r}_P \|, \\ {}_I\boldsymbol{e}_r^H &= \left(e_{r,x}^I \; 0 \; e_{r,z}^I \right)^T = {}_I\boldsymbol{r}_{p,r} - {}_I\boldsymbol{r}_R / \| {}_I\boldsymbol{r}_{p,r} - {}_I\boldsymbol{r}_R \|. \end{aligned} \tag{25}$$

Note that the position vectors $\boldsymbol{r}_{p,l}$ and $\boldsymbol{r}_{p,r}$, which denote the points where the tendons run onto the corresponding pulley, depend on $\boldsymbol{r}_Q$ and θ_L.

Within the identification process in Sect. 2.4, instead of the tendon forces and the gravity forces, an external force ${}_I\boldsymbol{F}_{\text{id}}^H \in \mathbb{R}^3$ is exerted at point Q whose virtual work is

$$\delta W^{\text{ext,id}} = {}_I\boldsymbol{F}_{\text{id}}^H \delta\boldsymbol{r}_Q. \tag{26}$$

The principle of virtual work (15) with the contributions (18), (22) and (24) corresponds to a weak variational expression of a nonlinear ordinary differential equation which can be obtained by integration by parts of (18). Since this ODE cannot be solved analytically, we introduce in the subsequent section the finite element method discretizing (15) in the sense of Bubnov-Galerkin. In doing so, we reduce an infinite dimensional system to a finite dimensional one.

2.3 Finite Element Method

Aiming for linear Lagrangian shape functions, the parameter space of ν, i.e. $[0, L]$, is divided by the nodes $n^1 = 0 < \ldots < n^e < \cdots < n^{k_{el}+1} = L$ into k_{el} element sets $\Omega_e = [n^e, n^{e+1}]$. Using the relation

$$\nu^e(\nu) = \frac{2}{n^{e+1} - n^e}(\nu - n^e) - 1, \tag{27}$$

it is convenient to introduce in every element set Ω_e the element coordinate $\nu^e \in [-1, 1]$. Then the generalized position function x is approximated by the linear interpolation of the nodal coordinates $x^e = x(n^e)$. Accordingly the position function takes the form

$$x(\nu) = \sum_{e=1}^{k_{el}} \chi_{\Omega_e}(\nu) \boldsymbol{N}(\nu^e(\nu))^T \begin{pmatrix} x^e \\ x^{e+1} \end{pmatrix}, \tag{28}$$

where χ_{Ω_e} is the characteristic function being one for $\nu \in \Omega_e$ and zero elsewhere and

$$\boldsymbol{N}(\nu^e) = 0.5 \; (\, 1 - \nu^e \;\; 1 + \nu^e \,)^T \tag{29}$$

corresponds to the linear shape function which linearly interpolates two subsequent nodal coordinates. The generalized position functions z and θ are approximated analogously such that the continuous formulation can be represented by the finite set of coordinates

$$\boldsymbol{q} = \left(x^1 \; z^1 \; \theta^1 \; \cdots \; x^{k_{el}+1} \; z^{k_{el}+1} \; \theta^{k_{el}+1}\right)^T. \tag{30}$$

The element connectivity matrix $\boldsymbol{C}_x^e \in \mathbb{R}^{3(k_{el}+1)\times 2}$ being defined by

$$\boldsymbol{q}_x^e = \left(x^e \;\; x^{e+1} \right)^T = (\boldsymbol{C}_x^e)^T \boldsymbol{q} \tag{31}$$

extracts from the generalized coordinates $\boldsymbol{q}$ the relevant coordinates for the linear interpolation within one element. Besides the analogous definition for z and θ, we introduce also the connectivity matrix $\boldsymbol{C}^L \in \mathbb{R}^{3(k_{el}+1)\times 3}$ given by

$$\boldsymbol{q}^{k_{el}+1} = \left(x^{k_{el}+1} \;\; z^{k_{el}+1} \;\; \theta^{k_{el}+1} \right)^T = (\boldsymbol{C}^L)^T \boldsymbol{q}. \tag{32}$$

Applying the chain rule together with (27), the derivative of (28) with respect to ν is obtained as

$$x'(\nu) = \sum_{e=1}^{k_{el}} \chi_{\Omega_e}(\nu) \boldsymbol{N}'(\nu^e(\nu))^T \frac{2}{\Delta L^e} \boldsymbol{q}_x^e \tag{33}$$

with $\boldsymbol{N}' = (\,-0.5 \;\; 0.5\,)^T$ and $\Delta L^e = n^{e+1} - n^e$. Moreover, the approximation (28) induces together with (31) also

$$\begin{aligned}\delta x(\nu) &= \sum_{e=1}^{k_{el}} \chi_{\Omega_e}(\nu) \boldsymbol{N}(\nu^e(\nu))^T (\boldsymbol{C}_x^e)^T \delta\boldsymbol{q},\\ \delta x'(\nu) &= \sum_{e=1}^{k_{el}} \chi_{\Omega_e}(\nu) \boldsymbol{N}'(\nu^e(\nu))^T \frac{2}{\Delta L^e} (\boldsymbol{C}_x^e)^T \delta\boldsymbol{q}.\end{aligned} \tag{34}$$

Providing the same computations for z and θ, the virtual work of the internal forces (18) is approximated by inserting (33) and (34). Together with a change of coordinates in the respective integral expression, we then obtain

$$\begin{aligned}\delta W^{\text{int}} &= \delta\boldsymbol{q}^T \sum_{e=1}^{k_{el}} \left[\boldsymbol{C}_x^e \boldsymbol{f}_x^{\text{int},e} + \boldsymbol{C}_z^e \boldsymbol{f}_z^{\text{int},e} + \boldsymbol{C}_\theta^e \boldsymbol{f}_\theta^{\text{int},e}\right]\\ &= \delta\boldsymbol{q}^T \boldsymbol{f}^{\text{int}},\end{aligned} \tag{35}$$

where

$$\begin{aligned}\boldsymbol{f}_x^{\text{int},e} &= -\int_{-1}^{1} \boldsymbol{N}' n_x^I d\nu^e, \;\; \boldsymbol{f}_z^{\text{int},e} = -\int_{-1}^{1} \boldsymbol{N}' n_z^I d\nu^e,\\ \boldsymbol{f}_\theta^{\text{int},e} &= -\int_{-1}^{1} \boldsymbol{N}' M + \boldsymbol{N}\left(x' n_z^I - z' n_x^I\right) \frac{\Delta L^e}{2} d\nu^e,\\ \boldsymbol{f}^{\text{int}} &= \sum_{e=1}^{k_{el}} \left[\boldsymbol{C}_x^e \boldsymbol{f}_x^{\text{int},e} + \boldsymbol{C}_z^e \boldsymbol{f}_z^{\text{int},e} + \boldsymbol{C}_\theta^e \boldsymbol{f}_\theta^{\text{int},e}\right].\end{aligned} \tag{36}$$

Note that the approximation of the position functions are also used within the evaluation of n_x^I, n_z^I and M which is why $\boldsymbol{f}^{\text{int}} = \boldsymbol{f}^{\text{int}}(\boldsymbol{q})$ is a nonlinear vector valued function. All integral expressions are evaluated numerically using Gauss quadrature. The discretization of the external virtual work due to gravity (22) leads to

$$\delta W^{\text{ext,g}} = \delta\boldsymbol{q}^T \boldsymbol{f}^{\text{ext,g}}, \tag{37}$$

where

$$\begin{aligned}\boldsymbol{f}^{\text{ext,g}} &= -\sum_{e=1}^{k_{el}} \boldsymbol{C}_x^e \rho A g \int_{-1}^{1} \boldsymbol{N} \frac{\Delta L^e}{2} d\nu^e\\ &\quad - m_H g\, \boldsymbol{C}^L \begin{pmatrix} 1 \\ 0 \\ ({}_I\boldsymbol{e}_x^I)^T \left({}_I\boldsymbol{e}_y^H \times (h\, {}_I\boldsymbol{e}_x^H + b\, {}_I\boldsymbol{e}_z^H)\right)\end{pmatrix}.\end{aligned} \tag{38}$$

Using (32), the discretization of the virtual work of the tendon forces (24) is

$$\delta W^{\text{ext,t}} = (\delta\boldsymbol{q}^{k_{el}+1})^T \boldsymbol{P}\boldsymbol{\lambda} = \delta\boldsymbol{q}^T \boldsymbol{C}^L \boldsymbol{P}\boldsymbol{\lambda} \tag{39}$$

with the tendon coupling matrix

$$\boldsymbol{P} = \begin{pmatrix} e_{l,x}^I & e_{r,x}^I \\ e_{l,z}^I & e_{r,z}^I \\ d({}_I\boldsymbol{e}_y^H)^T {}_I\boldsymbol{e}_z^H \times {}_I\boldsymbol{e}_l & -d({}_I\boldsymbol{e}_y^H)^T {}_I\boldsymbol{e}_z^H \times {}_I\boldsymbol{e}_r \end{pmatrix}. \tag{40}$$

Using (35), (37) and (39) in the principle of virtual work (15), the infinite dimensional variational expression is reduced to the finite dimensional expression

$$\delta\boldsymbol{q}^T \left(\boldsymbol{f}^{\text{int}} + \boldsymbol{f}^{\text{ext,g}} + \boldsymbol{C}^L \boldsymbol{P}\boldsymbol{\lambda}\right) = 0 \quad \forall \delta\boldsymbol{q}_{\text{adm}} \tag{41}$$

which induces a nonlinear vector valued equation which can be solved numerically.

2.4 Identification of the stiffness parameters

In this section, the experimental identification process is discussed in which the stiffness parameters EA, GA and EI for the constitutive laws (19) are identified. Two different experiments are carried out to excite independently the axial stiffness EA as well as the shear and bending stiffness GA and EI, respectively.

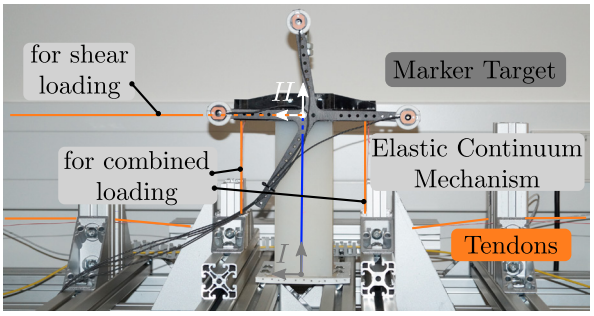

Fig. 2. Planar testbed used for the identification process.

The elastic parameters are incorporated in the FEM model being described by a nonlinear function. Thus, a nonlinear least square optimization is applied for the identification process using the "lsqnonlin" routine from MATLAB. Within this nonlinear optimization, the error function $\boldsymbol{\Delta}(\boldsymbol{\xi}) \in \mathbb{R}^m$, is minimized to find the desired parameters $\boldsymbol{\xi} \in \mathbb{R}^p$,

$$\min_{\boldsymbol{\xi}} ||\boldsymbol{\Delta}(\boldsymbol{\xi})||_2^2, \tag{42}$$

where $m, p \in \mathbb{R}$ are the number of measurements and the number of identified parameters, respectively. The identification process is performed for $k_{el} = 20$ number of elements.

Compression test for identification of EA In the compression test, a cylindrical specimen made of silicon is compressed up to 20% of the undeformed length L. The test is conducted for two different lengths $L = [28\text{mm}, 40\text{mm}]$. The measured quantities are the axial force f_x [N] and the displacement ΔL [m] which are illustrated in Fig. 3 as a stress-strain diagram with the axial stress $\sigma_x = \frac{f_x}{A}$ and the axial strain $\gamma_x^C = \frac{\Delta L}{L}$. For $\boldsymbol{\xi} = EA$, the error function used for the identification is

$$\boldsymbol{\Delta}(EA) = (\,\tilde{x}_1 - x_1(EA) \;\ldots\; \tilde{x}_m - x_m(EA)\,)^T, \tag{43}$$

where $\tilde{x}_i$ is the measured and $x_i(EA)$ is the computed axial position for an external force

$${}_I\boldsymbol{F}_{\text{id}}^H = (\,-f_x \;\; 0 \;\; 0\,)^T \tag{44}$$

with the virtual work contribution (26). In the left diagram of Fig. 3, a clear nonlinearity in the measured stress-strain curve (red curve) can be observed, which can be reproduced much better by the Neo-Hookean material law (19) than by the linear Hookean law. Tab. 1 shows that the linear Hookean law overestimates the stiffness of the specimens.

Table 1. Left: Identified EA for Hookean and Neo-Hookean material laws. Right: Identified GA and EI.

compression			shear		
L [mm]	EA_{nH} [N]	EA_H [N]	$f_{t,max}$	GA [N]	EI [Nm^2]
28	7448.94	8972.10	33 N	2405	2.993
40	7591.09	9071.84	66 N	2422	3.003

Shear test for identification of GA and EI For the shear test, a force in $\boldsymbol{e}_z^I$-direction is applied at the tip of the ECM as depicted in Fig. 2 which leads to a bending deformation about the $\boldsymbol{e}_y^I$-axis and a shear deformation along the $\boldsymbol{e}_z^I$-axis. For all displacements increments, the

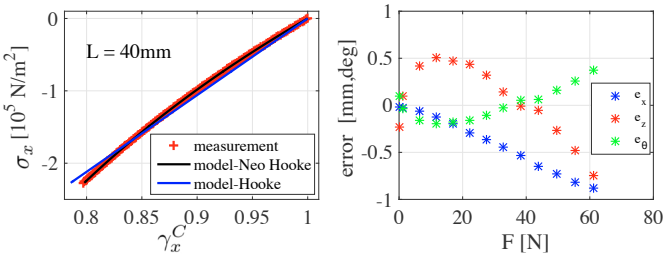

Fig. 3. Left: Identification of EA. Right: Error of the position e_x, e_z and orientation e_θ in the shear test between measured and modeled data.

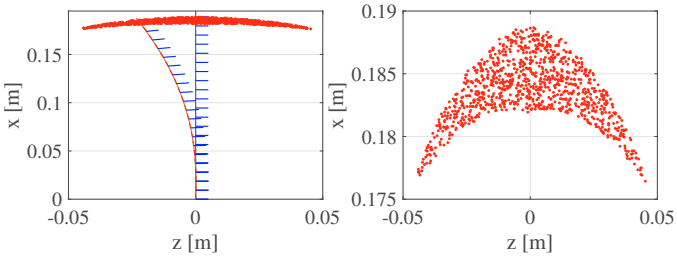

Fig. 4. Workspace $\mathcal{P}$ with close-up view (right) of the planar ECM for 1000 randomly applied tendon forces $(\lambda_l,\ \lambda_r)$ in the range of [0N-160N].

position and orientation are measured by a camera as well as the applied tendon force. The identified value $EA = 7500$[N] from the compression test is used within the shear test as an initial guess for the bending stiffness $EI = 7500/A \cdot I = 871080 \cdot I$ [Nm^2] with second moment of area I. Here, $\boldsymbol{\xi} = (\,GA\ EI\,)^T \in \mathbb{R}^2$ and the error function for the identification is

$$\boldsymbol{\Delta}(\boldsymbol{\xi}) = \left(\,\tilde{z}_1 - z_1(\boldsymbol{\xi})\ \tilde{\theta}_1 - \theta_1(\boldsymbol{\xi})\ \ldots\ \tilde{z}_m - z_m(\boldsymbol{\xi})\ \tilde{\theta}_m - \theta_m(\boldsymbol{\xi})\,\right)^T,$$

where $\tilde{z}_i$, $\tilde{\theta}_i$ are the measured and z_i, θ_i are the computed z-position and tip angle for the external force

$$_I\boldsymbol{F}^H_{\text{id}} = (\,0\ 0\ f_t\,)^T. \tag{45}$$

The results of the identification procedure are depicted in Fig. 3 and in Tab. 1.

3. POLYNOMIAL MODEL

As mentioned in the Introduction, an abstract modeling approach based on polynomials is suggested by [2] for a model-based control approach for an ECM. The model considers that the mapping from the Cartesian pose $(x_L, z_L, \theta_L) \in \mathbb{R}^3$ in the workspace $\mathcal{P}$ to an associated Cartesian wrench applied at the head $_I\boldsymbol{h}^H \in \mathbb{R}^3$ which is necessary to deflect the ECM into this configuration, can be represented by a polynomial function. In [3], a method for the identification of such a mapping is proposed and the results show that polynomials of order 3 provide the best match for simulation and experimental data. For each wrench component $(h_1\, h_2\, h_3)^T = (f_x\, f_z\, \tau_y)^T$, a multivariate polynomial mapping of the form

$$h_j = \boldsymbol{x}^T\boldsymbol{\beta}_j, \quad j = 1, 2, 3, \tag{46}$$

is identified, where $\boldsymbol{\beta}_j \in \mathbb{R}^{20}$ represents the polynomial coefficients for the j-th wrench component and $\boldsymbol{x} \in \mathbb{R}^{20}$ is

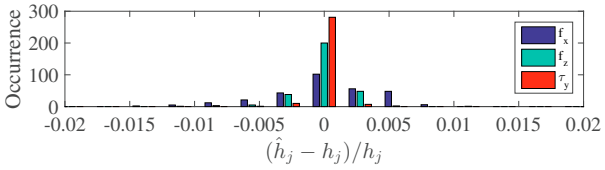

Fig. 5. Histogram of e_{rel} computed with 300 testing points.

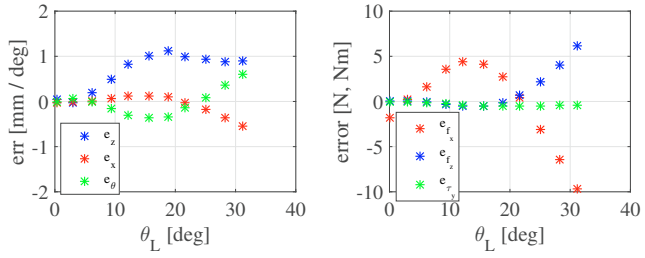

Fig. 6. Left: Error of the computed head position by the FEM model and the measured head position for a positive bending motion. Right: Error of the predicted wrench from the polynomial map and measured head wrench for all wrench components.

$$\boldsymbol{x} = (1\quad x_L\quad z_L\quad \theta_L\quad (x_L)^2\quad x_L z_L\quad \cdots (\theta_L)^2 \cdots (x_L)^3\quad (x_L)^2 z_L\quad \cdots\quad x_L z_L \theta_L\quad \cdots\quad (\theta_L)^3)^T. \tag{47}$$

To find the coefficients via a polynomial regression according to [10], the training set $\mathcal{C}$ with 1000 poses is calculated using the calibrated FEM model from the former section. The input of the FEM simulation is a random wrench from the set

$$\{\boldsymbol{h} \in \mathbb{R}^3 | \boldsymbol{h}_{min} < \boldsymbol{h} < \boldsymbol{h}_{max}\}, \tag{48}$$

with $\boldsymbol{h}_{max} = [20,\ 80,\ 11]$ and $\boldsymbol{h}_{min} = [-330,\ -80,\ -11]$. The maximum and minimum values are chosen to ensure that the training set $\mathcal{C}$ covers well the reachable workspace $\mathcal{P}$ of the ECM, see Fig. 4.

To evaluate the accuracy of the polynomial model, 300 data pairs from $\mathcal{C}$ are randomly chosen to serve as the test set. The relative error distribution of each h_j of a 3-degree polynomial regression model is depicted in Fig. 5, in which $\hat{h}_j$ and h_j denote the estimated and the observed value of the polynomial model. The vertical axis represents the amount of prediction points referred to a prediction error level. Most of the predicted wrench components have a relative error less than 0.02. The points with relative error beyond the interval $[-0.02, 0.02]$ are not displayed as located in a small range around zero (from -2[N] to 2[N] for the force and from -0.2[Nm] to 0.2[Nm] for the torque).

4. COMPARISON

This section will compare the two established models regarding there prediction accuracy and computation time. For the evaluation, we use experimental data from the planar testbed where a combined loading is applied, i.e. the mechanism is moved with two antagonistically arranged tendons, cf. Fig. 2. As the established models are static ones, the data is measured at poses in static equilibrium.

4.1 Accuracy

The accuracy of the FEM model is mainly dependent on the identified material parameters provided that the assumptions about the geometry of the deformation and the

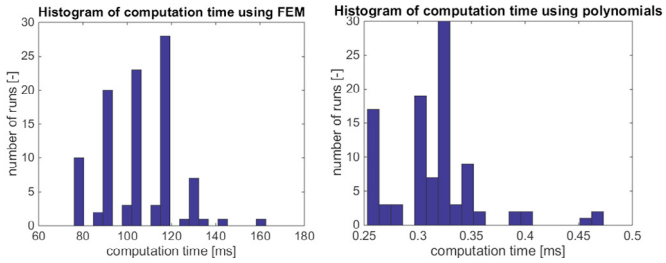

Fig. 7. Histograms of the computational time used by the FEM model (left) and the polynomial model (right) computed with 100 randomly selected poses from $\mathcal{C}$.

applied material laws match well. In Fig. 6, a comparison is shown between static poses of simulated and measured data. The input to the FEM model are the measured tendon forces $\boldsymbol{\lambda}$ for which (x_L, z_L, θ_L) is computed and compared with the measured head pose by the camera system. The left plot of Fig. 6 states, that the errors stay below 5% with respect to the measured workspace (z: 2.6%, x: 4.7%, θ: 1.8%) yielding an accurate model.
To evaluate the accuracy of the polynomial model, the same measured data is used, however, the input is the measured head-pose to compute the associated head wrench. The measured head wrench is computed based on the measured tendon forces and the tendon coupling matrix $\boldsymbol{P}$ introduced in (40). The results are depicted in the right of Fig. 6. Compared with the accuracy of the FEM model, the polynomial model is less accurate (x: 9.4% z: 11.6% θ: 9.7%).

4.2 Computational Efficiency

As stated in the motivation, a primary goal of the identified mapping is to be computationally efficient for the use in real time control. To investigate the computational efficiency, 100 pose-wrench pairs are randomly selected from $\mathcal{P}$ and are used as input of the polynomial model and the FEM model and the computational time of each model is measured. Fig. 7 depicts the histogram of the computation time, which states that the polynomial model is at least 200 times faster than the FEM model.

4.3 Discussion

Both models prove to represent the deformation characteristic of the tendon-driven ECM. The FEM model is more accurate but needs more time for one simulation run. By reducing the number of elements, this computation time can be decreased and it is an open research question in this field to which extend the number of elements can be reduced without losing accuracy. Also, more sophisticated shape functions can be applied which incorporate the characteristic of a deformed center line. By that, it could be possible to reduce the number of elements still achieving high accuracy.
The polynomial model is computationally fast but lacks accuracy. To increase the accuracy, the polynomial model can be experimentally trained to match the real system as proposed in [3]. However, maximum model errors of 11% are still in a very good range. From a modeling perspective, it should be investigated the validity of the assumption that the deformation of the ECM can be described by (x_L, z_L, θ_L) only.

5. CONCLUSION

In this work, two models are investigated to simulate the static deformation of a tendon-driven elastic continuum mechanism. At first, a nonlinear FEM model is setup and the parameters are experimentally identified. The incorporated geometry of the deformation matches well the real system. Furthermore, it could be observed during the experiments that a Neo-Hookean material law for the axial compression needs to be implemented to generate an accurate model. To the authors knowledge, this is the first time that a FEM model with nonlinear material law and nonlinear tendon-coupling is applied for simulation and identification of a tendon-driven ECM. In the future, the number of elements and alternative shape functions shall be identified to increase the computational efficiency.
The second model is based on multivariate polynomials which maps from the Cartesian head position of the ECM to the associated wrench necessary for this deformation. The model proved to match the experimental platform well, however with less accuracy compared to the FEM model. In the future, the identification process in which the polynomial coefficients are found needs to be updated to incorporate that physical properties are displayed by the polynomial model, e.g. the symmetry of the associated stiffness matrix. This property could be incorporated in the identification process which would benefit from a reduction of the to be identified polynomial coefficients.

REFERENCES

[1] D. Camarillo, C. Carlson, and J. Salisbury. Configuration Tracking for Continuum Manipulators With Coupled Tendon Drive. *IEEE Transactions on Robotics*, 25(4):798–808, Aug. 2009.
[2] B. Deutschmann, A. Dietrich, and C. Ott. Position control of an underactuated continuum mechanism using a reduced nonlinear model. In *Decission and Control (CDC), IEEE International Conference on*. IEEE, 2017.
[3] B. Deutschmann, T. Liu, A. Dietrich, and C. Ott. A method to identify the nonlinear stiffness characteristics of an elastic continuum mechanism. *accepted in IEEE Robotics and Automation Letters (RA-L)*, 2018.
[4] S. R. Eugster. *Geometric Continuum Mechanics and Induced Beam Theories*. Springer, 2015.
[5] V. Falkenhahn, T. Mahl, A. Hildebrandt, R. Neumann, and O. Sawodny. Dynamic modeling of bellows-actuated continuum robots using the euler–lagrange formalism. *IEEE Transactions on Robotics*, 31(6):1483–1496, 2015.
[6] M. Giorelli, F. Renda, M. Calisti, A. Arienti, G. Ferri, and C. Laschi. Neural Network and Jacobian Method for Solving the Inverse Statics of a Cable-Driven Soft Arm With Nonconstant Curvature. *IEEE Transactions on Robotics*, 31(4):823–834, 2015.
[7] I. A. Gravagne, C. D. Rahn, and I. D. Walker. Large deflection dynamics and control for planar continuum robots. *Transactions on Mechatronics, IEEE/ASME*, 8(2):299–307, 2003.
[8] J. Reinecke, B. Deutschmann, and D. Fehrenbach. A structurally flexible humanoid spine based on a tendon-driven elastic continuum. In *Robotics and Automation (ICRA), 2016 IEEE International Conference on*, pages 4714–4721. IEEE, 2016.
[9] D. C. Rucker and R. J. Webster III. Statics and dynamics of continuum robots with general tendon routing and external loading. *IEEE Transactions on Robotics*, 27(6):1024–1030, 2011.
[10] M. Shacham and N. Brauner. Minimizing the effects of collinearity in polynomial regression. *Industrial & engineering chemistry research*, 36(10):4405–4412, 1997.